Synergy of strengthening and toughening of a nanoprecipitate-strengthened steel

Xinghao Wei[1], Xue Cao[2, *], J.H. Luan[3] , Z. B. Jiao[4] , C. T. Liu[3] and Z. W. Zhang[1, 5*]

[1]*Key Laboratory of Superlight Materials and Surface Technology, Ministry of Education, College of Materials Science and Chemical Engineering, Harbin Engineering University, Harbin 150001, China*

[2] *College of Computer Science and Technology, Harbin Engineering University, Harbin 150001, PR China*

[3] *Department of Materials Science Engineering, College of Science and Engineering, City University of Hong Kong, Hong Kong, China*

[4]*Department of Mechanical Engineering & Shenzhen Research Institute, The Hong Kong Polytechnic University, China*

[5]*Iron & Steel Research Institute of Ansteel Group Corporation, Anshan 114009, Liaoning, China*

* Corresponding Authors, Email: caoxuer@hrbeu.edu.cn (Xue Cao); zwzhang@hrbeu.edu.cn (Z. W. Zhang)

Abstract

A high strength steel with a combination of ~930 MPa yield strength

and excellent low temperature toughness with an upper shelf energy of above 200 J and ductile brittle transition temperature (DBTT) of lower than −90 °C, are developed. The strengthening and toughening mechanisms are investigated systematically based on the detailed characterization on microstructures including matrix and precipitates. The results indicate that the steel is composed of fine lath martensite with nanoscale rod-like Cu precipitates. The strength is contributed by a combination of solid-solution strengthening, dislocation strengthening, grain boundary strengthening and precipitation strengthening of nanoscale Cu-precipitates. The instrumented Charpy impact results indicated that the crack propagation is the main factor affecting DBTT while the dislocation density has an obvious effect on both crack initiation and propagation. Fine lath structure of low carbon martensite increases the crack resistance and delay the rapid unstable crack propagation at low temperatures. The strengthening and toughening are discussed in details.

Keywords: Nanoprecipitate-strengthened steel, Ductile-brittle transition, Impact toughness, Crack propagation, Strengthening mechanisms.

1. Introduction

High-strength low-alloy (HSLA) steels have good strength–toughness combination and excellent weldability, which can be widely applied to

shipbuilding, marine engineering equipment, bridge construction, oil pipeline, etc. [1-3]. The microstructure components of low carbon HSLA steels can be tuned to include one or more of three common microconstituents: polygonal or acicular ferrite, low-carbon bainite and lath martensite [4]. The quenched martensite is an unstable structure and its high dislocation density results in a relative low plasticity even though for low carbon martensite. Thus, tempering treatments are required to optimize the overall performance of the martensitic steels [5-7].

The decrease in dislocation density after tempering will lead to a decrease in yield strength. Precipitation strengthening can be designed to enhance the tempered low carbon martensite in HSLA steels [8]. In general, aging temperatures from 450−650 °C are applied to induce the precipitates in most HSLA steels. This temperature range is the same with the tempering temperatures of the quenched martensite. Thus, the aging and tempering processes are combined together, two in one for technical operation. Aging process controls the expected precipitate size and number density to improve the strength [9-14]. It has been found that a high yield strength of up to 1700 MPa could be achieved in a Fe-0.008C-1.5Mn-2.5Cu-4Ni-1Al-1.5W (wt.%) steel. Cu-enriched precipitates provide more than 700 MPa yield strength through precipitation strengthening mechanism after aging at 500 °C for 5 h [11].

Aging at 450−550 °C can greatly improve the strength, but it is often

accompanied by a decrease in toughness [1, 4, 14, 15]. In some steels, element segregation occurs during aging at 350−550 °C, and impurity elements segregate at grain boundaries, leading to intergranular fracture [16, 17]. D. Jain et al. found that tempering martensite can cause the formation and coarsening of cementite, which can initiate brittle fracture [18, 19]. Another study suggested that the martensite tempering can cause the thermal decomposition of interlath retained austenite and the coarsening of a large amount of interlath cementite, resulting in the decrease of toughness [8]. Besides, in the process of aging treatment, lath martensite may change to polygonal morphology and lose the hierarchical structure of lath martensite [18]. It was found that improper copper content leads to segregation of copper at grain boundaries and results in grain boundary embrittlement [20, 21]. Due to the above reasons, it is difficult to obtain high strength and excellent toughness simultaneously.

Recently, H.J. Kong et al. chose high aging temperature of 640 °C to avoid the temper embrittlement regime, and obtained a steel with a yield strength of ~900 MPa and impact energy of 200 J at −40 °C while with a low elongation of ~12% due to the introduction of the cold rolling process [22]. Z.J. Xie et al. used a two-step intercritical heat treatment to control the content of retained austenite to around 10% in lath martensite and obtained an impact energy of 65 J at −80 °C in a steel [23]. However, the yield strength is only 540 MPa due to the high content of austenite. L.Y.

Kan et al. found that the addition of Ti can promote the precipitation of Cu-rich precipitates and increase the content of high-angle grain boundaries (HAGBs) in HSLA steels. A high impact energy of 132 J at −40 °C were obtained at a yield strength of 1055 MPa [24]. However, to date it is seldom reported that an excellent low temperature toughness with the DBTT of lower than -90 °C can be obtained in a steel with the yield strength greater than 900 MPa.

In this work, a high-strength steel with a combination of high strength, ductility, and superior low-temperature impact toughness were developed by proper control of the fine lath martensite structure along with the Cu-rich nanoscale precipitation. The DBTT and crack propagation during Charpy impacting were investigated in detail. The effects of dislocation density on crack initiation, crack propagation and low-temperature toughness were systematically investigated. The strengthening and toughening mechanisms are also discussed.

2. Materials and methods

The composition of the nanoprecipitate-strengthened steel is list in Table 1. The steel was prepared via melting high purity elements in a vacuum induction furnace under argon atmosphere. The as-cast ingot was homogenized at 1200 °C for 20 h and then hot rolled to 25 mm followed by water quenching. These hot-rolled samples were solution-treated at 900

°C for 50 min and then water quenched (labeled as SS). The SS samples were then aged at 525 °C for 25 h and followed by air cooling (AG525). In order to quantitatively evaluate dislocation density by XRD, a reference sample (labeled as RS) was prepared through complete annealing at 1000 °C for 1 h by furnace cooling and stress relief annealing at 750 °C for 10 h by furnace cooling.

Table 1. Chemical composition of the steel (wt.%)

C	Si	Mn	Mo	Cu	Ni	Cr	Nb + Ti
0.048	0.25	0.9	0.5	1.3	3.0	0.55	0.04-0.07

Tensile tests were conducted using an INSTRON 5565 testing machine with a strain rate of 1.3×10^{-3}/s at room temperature. An extensometer with a gage length of 25 mm was applied. Tensile tests were repeated thrice for each sample. The yield strength was determined at 0.2% offset.

The Charpy impact tests for determining toughness were carried out at various temperatures on a Zwick/Roell 450 J impact tester. Impact test specimens with dimension of 55×10×10mm were machined from the 1/2 thickness of the steel plates in the transverse direction. The V-notch were cut by electro discharge machine in the thickness direction according to the ASTM E23-18 standard. Prior to the testing, the specimens were immersed in a bath of a mixture of anhydrous ethyl alcohol and liquid nitrogen at 2 °C below the actual impact temperature for more than 20 min to ensure a

uniform temperature across the entire specimens. DBTT was estimated as a temperature corresponding to the half of the sum of the upper and lower shelf energy. Three samples were tested for each condition and the average value is reported. The error is determined by the standard deviation of the average.

The microstructures were characterized by transmission electron microscopy (TEM) and electron backscattered diffraction (EBSD). EBSD with orientation imaging microscope system was employed on a Hitachi S-3400N SEM to investigate the effective grain size and grain boundary characteristics. Phase identification was performed using X-ray diffraction on an X'Pert Pro X diffractometer with Cu K_a. The quantitative analyses of dislocation densities were performed based on the XRD data from the tested tensile samples using the Williamson-Hall method [25]. For this method, the following mathematical relation was used to relate the integral breadth (β), average domain size (D_V), and the microstrain (ε), and is given by:

$$\frac{\beta cos\theta}{\lambda} = \frac{1}{D_V} + 2\varepsilon(\frac{2Sin\theta}{\lambda}) \quad (1)$$

Regression analysis of the plot for $\beta cos/\lambda$ vs. $2sin\theta/\lambda$ gives the values of ε and D_V, from the slope and the ordinate intersection, respectively. The dislocation density, ρ, is calculated by the analyzing the microstrain through the following equation [26]:

$$\rho = \frac{k\varepsilon}{b^2} \quad (2)$$

where k is the material constant (14.4 for ferrite), and b is the Burger's vector of ferrite (0.284 nm).

Sharp needle-shaped specimens needed for APT analysis were prepared with lift-outs and annular milling in a FEI Scios focused ion beam/scanning electron microscope (FIB/SEM). APT was performed with a Cameca LEAP 5000 XR local electrode atom probe operated in a voltage pulse mode, with a pulse repetition rate of 200 kHz, a pulse fraction of 0.2, and a specimen temperature of 50 K.

3. Results

3.1 Mechanical Properties

The tensile properties of the SS and AG525 samples are plotted in Fig. 1(a). It can be seen that after a 50 min solution treatment at 900 °C followed by water quenching, the SS sample has a high yield strength of ~905 MPa and an ultimate strength of ~1134 MPa while keeping a ductility of ~15%. The AG525 sample shows a yield strength of ~927 MPa, an ultimate strength of ~950 MPa while the ductility increases to ~21%. These results indicate that the aging process increases the yield strength and elongation while gets the ultimate strength decreased.

The impact energy under various temperatures of the steel are plotted in Fig. 1(b). Boltzmann function fitting based on the experimental data was conducted to obtain the curves of the impact energy versus temperatures

[27]. The Boltzmann function can fit the toughness data very well with a coefficient of determination (R^2) greater than 0.998. The upper and lower shelf energy was determined as the value of impact energies measured at 0 ºC and −196 ºC, respectively. The upper shelf energy of SS and AG525 at 0 ºC is 229 and 216 J, respectively. When decreasing the temperature to −80 ºC, the absorbed energy of SS and AG525 remains at a high level. When the impact temperatures further drop to −100 ºC, the impact energy of SS and AG525 still keeps above 110 and 60 J, respectively. According to the results of regression analysis, the DBTT of SS and AG525 are estimated as −100 and −91 ºC, respectively.

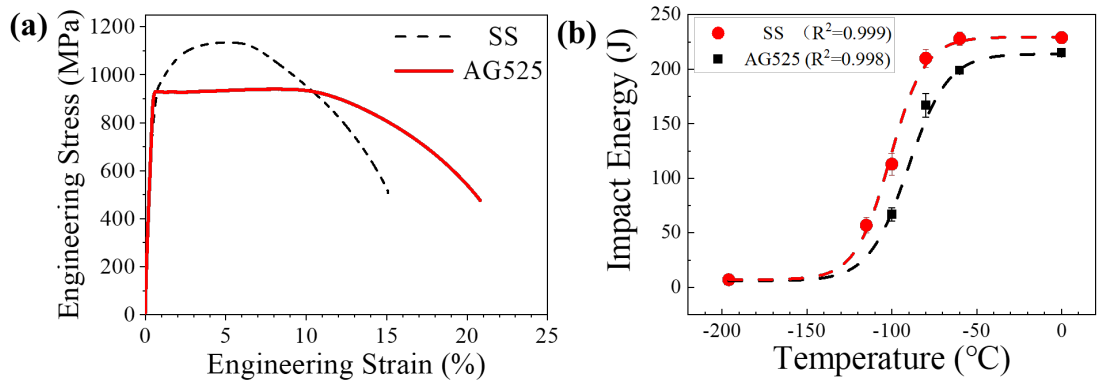

Fig. 1. Engineering tensile stress-strain curves (a) and impact energy vs. test temperatures along with the Boltzmann function fitting based on the experimental data (dash-line) (b).

The impact load and absorbed energy versus displacement of SS and AG525 at various temperatures are shown in Fig. 2. The corresponding crack initiation energy, crack propagation energy and total impact energy for SS and AG525 samples at various temperatures are summarized in Table 2. The data are obtained from instrumented impact experiments at

−60 ºC, −80 ºC, −100 ºC and −196 ºC, respectively. At −60 ºC, the curve of AG525 shown in Fig. 2a is a typical stable process for crack initiation and propagation in steel, including the initial elastic deformation, the occurrence of the general yield, the initiation of fracture crack at the peak load and the stable crack propagation period till the fracture. It is generally considered that the crack propagation roughly initiates at peak load [28]. Hence, the area before the peak load can be deemed to the crack initiation energy, which consists of elastic and plastic deformation stage, and the area from peak load to fracture is corresponding to the crack propagation energy [29]. It can be seen from Fig.2a that there is no general yield point in the curve of SS sample, which is similar to the result of engineering tensile stress-strain curve. It is obvious from Table 2 that the crack initiation energy of AG525 at −80 ºC is almost equal to that at −60 ºC. However, in the crack propagation period at −80 ºC, there is an obvious inflexion (pink point) in the curve, indicating the change in propagation from the stable to unstable state, as shown in Fig.2b. The slope of load curve within the unstable crack propagation period is much larger than that of stable crack propagation, and the total absorbed energy lost from −80 ºC to −60 ºC is mainly in the unstable stage. As for the sample impacted at −100 ºC, the crack unstable propagation occurs fast, leading to a decrease in the toughness. When the impact test temperature was decreased down to −196 ºC, the unstable crack propagation occurs immediately after the initial

elastic deformation for both SS and AG525 samples, leading to the very low impact energy of ~7 and ~9 J, respectively. It is clearly from Table 2 that, when decreasing the impact temperature down to −100 ºC, for both SS and AG525, the crack initiate energy remains unchanged while the total absorbed energy is determined by the propagation energy. When decreasing the impact temperature to −196 ºC, the crack initiate energy decreases abruptly and there is no absorbed energy contributed from the crack propagation period.

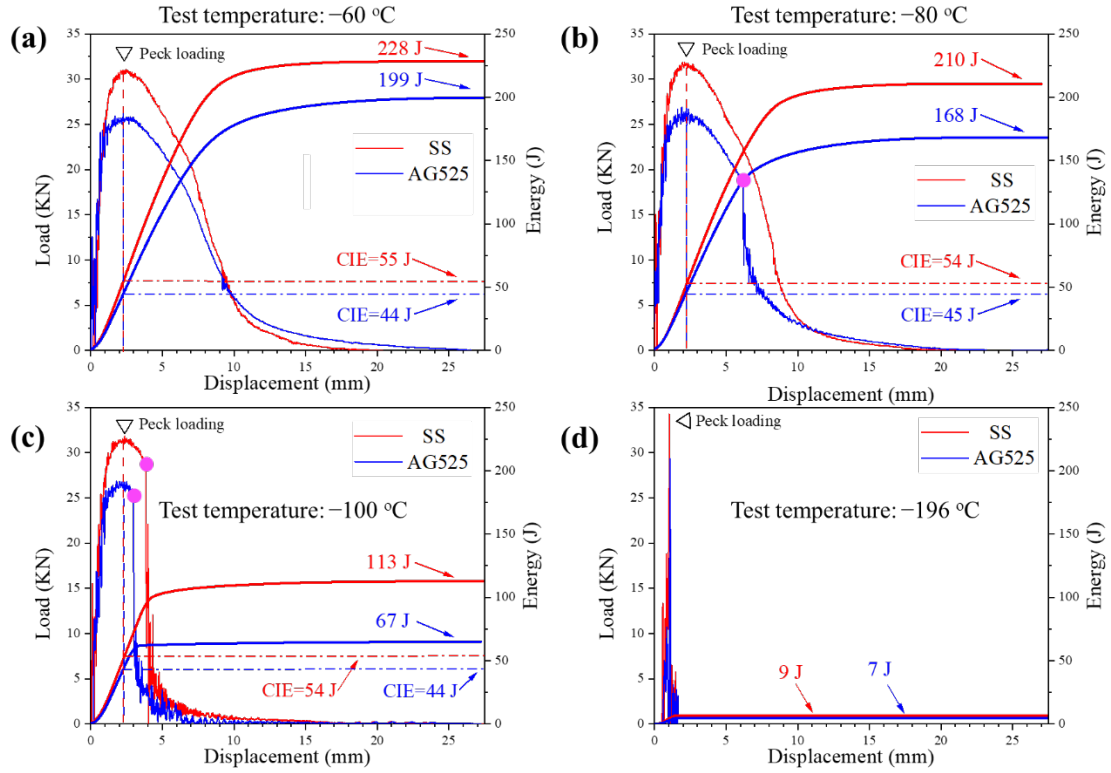

Fig. 2 The impact load and work curves versus displacement obtained from instrumented impact experiments of SS and AG525 at various temperatures: (a) −60 ºC, (b) −80 ºC, (c) −100 ºC, and (d) −196 ºC.

Table 2. The crack initiation energy, the crack propagation energy and total impact energy for SS and AG525 samples at various temperatures.

Temperature (ºC)	Crack initiate energy (J)		Crack propagation energy (J)		Total impact energy (J)	
	SS	AG525	SS	AG525	SS	AG525
−60	55	44	173	155	228	199

−80	54	45	156	123	210	168
−100	54	44	59	23	113	67
−196	9	7	0	0	9	7

3.2 fractographs

Fig. 3 demonstrates the fracture surfaces of the Charpy impact specimens of AG525 after impact fracture from −60 ºC to −196 ºC. According to the ASTM E23-18 standard, the fracture surface of a Charpy impact specimen consists of four regions. The fracture initiation region below the notch, the unstable fracture region in the center of the fracture surface, the shear lip regions near the edges of the specimen and the final fracture region on the opposite of the notch. The percentage of shear fracture (PSF) on the fracture surface is typically calculated by the ratio of the area of unstable fracture region and the total fractured area. The upper right corner of Fig. 3 shows the macro fracture morphology of Charpy impact specimens. It can be seen that as the temperature decreases, the unstable fracture region in fracture surface increases, which is consistent with the unstable propagation in Fig. 2. Dimple-like feature surface, a character of a ductile failure, is observed in the micrographs of the samples impacted at −60 ºC and −80 ºC. For the samples impacted at −80 ºC and −100 ºC (Fig. 3b and c), the impact fracture surfaces have a mixed feature combining quasi-cleavage and dimples. In Fig. 3b, 60% of the fracture surface is covered by dimples, while 40% by tearing edge of quasi-

cleavage fracture. For the sample impacted at −80 °C, most area of the fracture surface is covered by tearing edge of quasi-cleavage, and dimples are distributed only on the steps between part of the interface plane. For the sample impacted at −196 °C (Fig. 3d), the fracture plane is very flat and has almost no undulation, which is a typical cleavage transgranular failure. These results are in general qualitative agreement with the impact energy obtained at the corresponding temperatures.

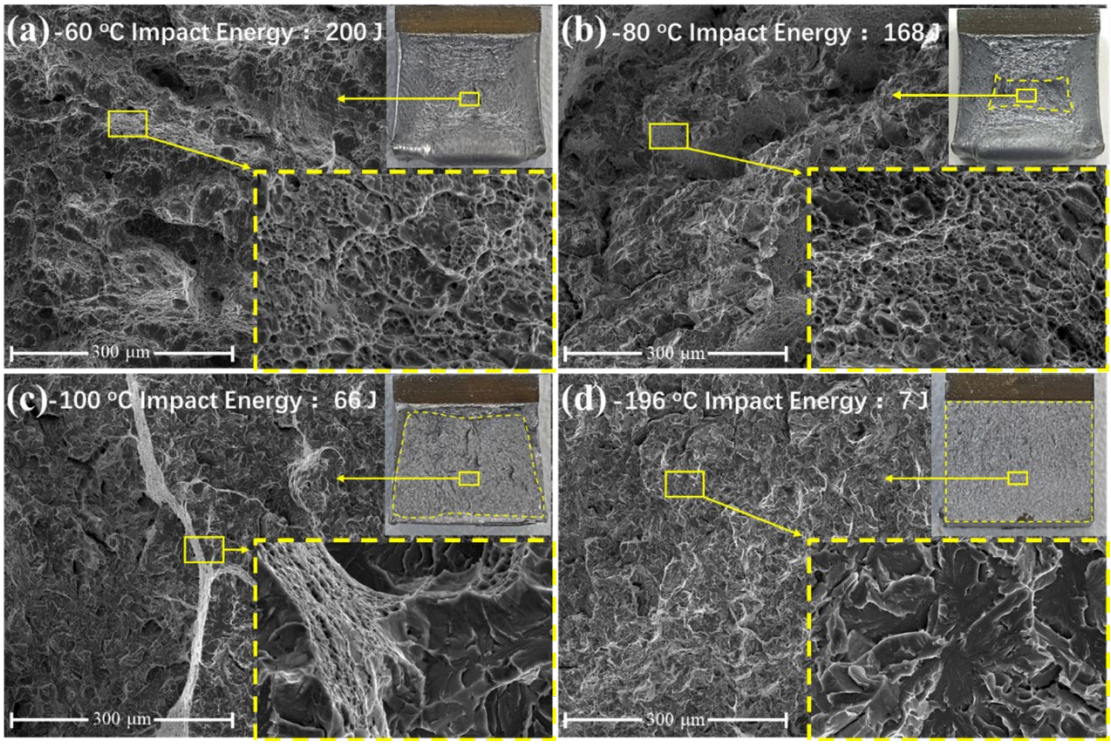

Fig. 3 Typical impact fracture surfaces of AG525 fractured at (a) −60 °C, (b) −80 °C, (c) −100 °C and (d) −196 °C.

3.3 Microstructure characterization

Microstructures of the SS and AG525 samples observed by SEM are shown in Fig. 4. After a full austenitization at 900 °C for 50 min and quenching in water, a fine lath martensitic microstructure is obtained in the

SS samples, as shown in Fig. 4a. Fig. 4b displays the microstructure of the AG525 steel. After aging at 525 °C for 25 h and air-cooling, the lath martensite was tempered. The lath structure of martensite in prior austenite grains is no longer clear, and the prior austenite grain boundaries are visible in the aged samples.

Fig. 4(c) illustrates the X-ray diffraction patterns of the SS, AG525 and RS samples. The patterns for all the three samples exhibit mainly three peaks, corresponding to the (110), (200) and (211) crystallographic plane of the bcc structure, respectively. Obviously, all of the samples are single phase martensite. No austenite and precipitation phases can be detected through XRD. Applying the values of ε obtained from Eq. (1), the ρ for SS and AG525 can be calculated by Eq. (2), and the values are 9.06×10^{14} and $4.84\times10^{14}\ m^{-2}$, respectively. These results indicate that aging induced a slight decrease in dislocation density.

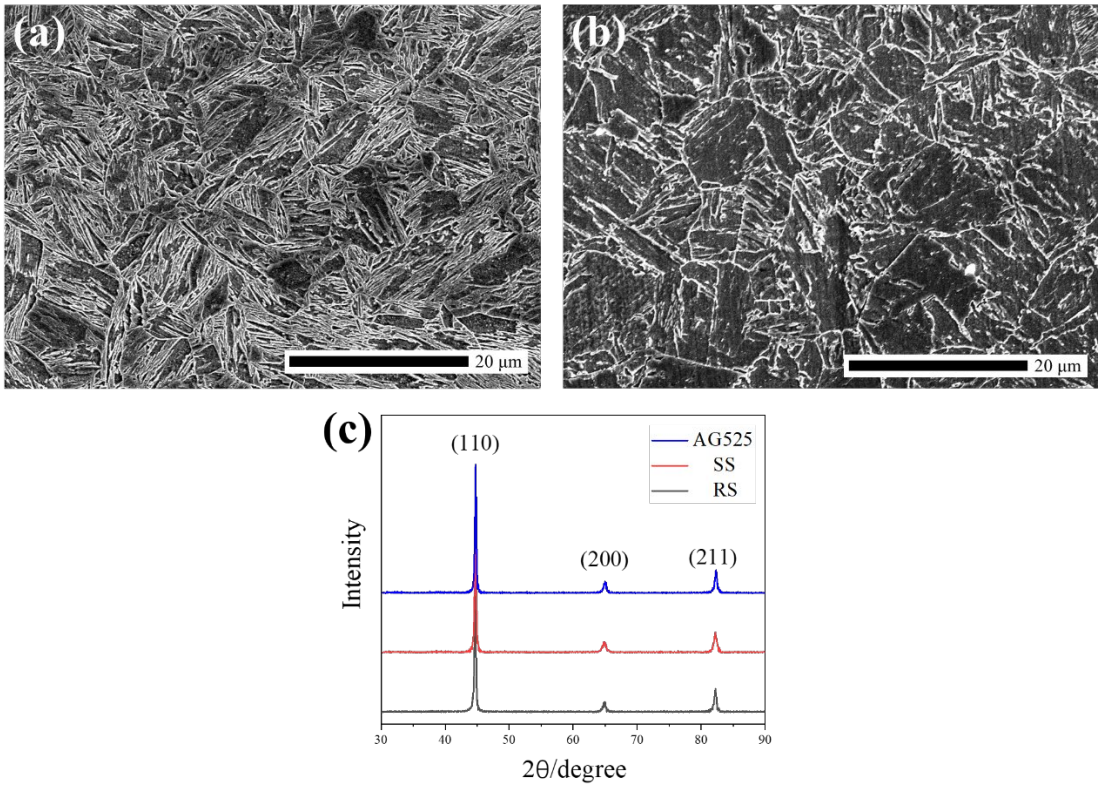

Fig. 4. SEM micrographs of (a) SS sample, (b) AG525 sample and the X-ray diffraction patterns of AG525, SS, RS steel.

To attain precise information on the microstructures of the steels, EBSD and TEM observations were carried out for the AG525, and the results are shown in Fig. 5. It can be seen from Fig. 5a that the tempered martensite in AG525 still retains the lath martensite structure. The misorientation map of grain boundaries and prior austenite grain boundaries are analyzed by EBSD (Fig. 5b). The black lines denote the HAGBs (misorientation (θ) > 15°) which compose of prior austenite grains, martensite packets and block boundaries. The green lines represent the low angle grain boundaries (LAGBs, misorientation (θ) < 5°), which mainly compose of lath boundaries. The grain boundaries in the range from 15° to 50° are plotted as black thick lines on the bottom left of the map. These

boundaries are considered to be the prior austenite grain boundaries [30, 31]. The average value of prior austenite grain size (PAGS) is 14.8 μm. Previous investigations have indicated that the HAGBs are able to promote the crack deflection during crack propagation and hinder the crack extension [32]. Therefore, the "block" size is identified as the effective grain size (EGS) in lath martensitic steel, for discussing their effects on both strength and toughness. Fig. 5c and 5d show the misorientation angle distribution of grain boundaries and grain size distribution for AG525. The average angle is 25.3° and the EGS is evaluated as 3.6 μm for AG525. Fig. 5e shows the fine lath structure of the AG525 steel. After aging at 525 °C for 25 h, the AG525 still has the typical elongated lath martensite morphology and quite fine lath width of ~90 nm.

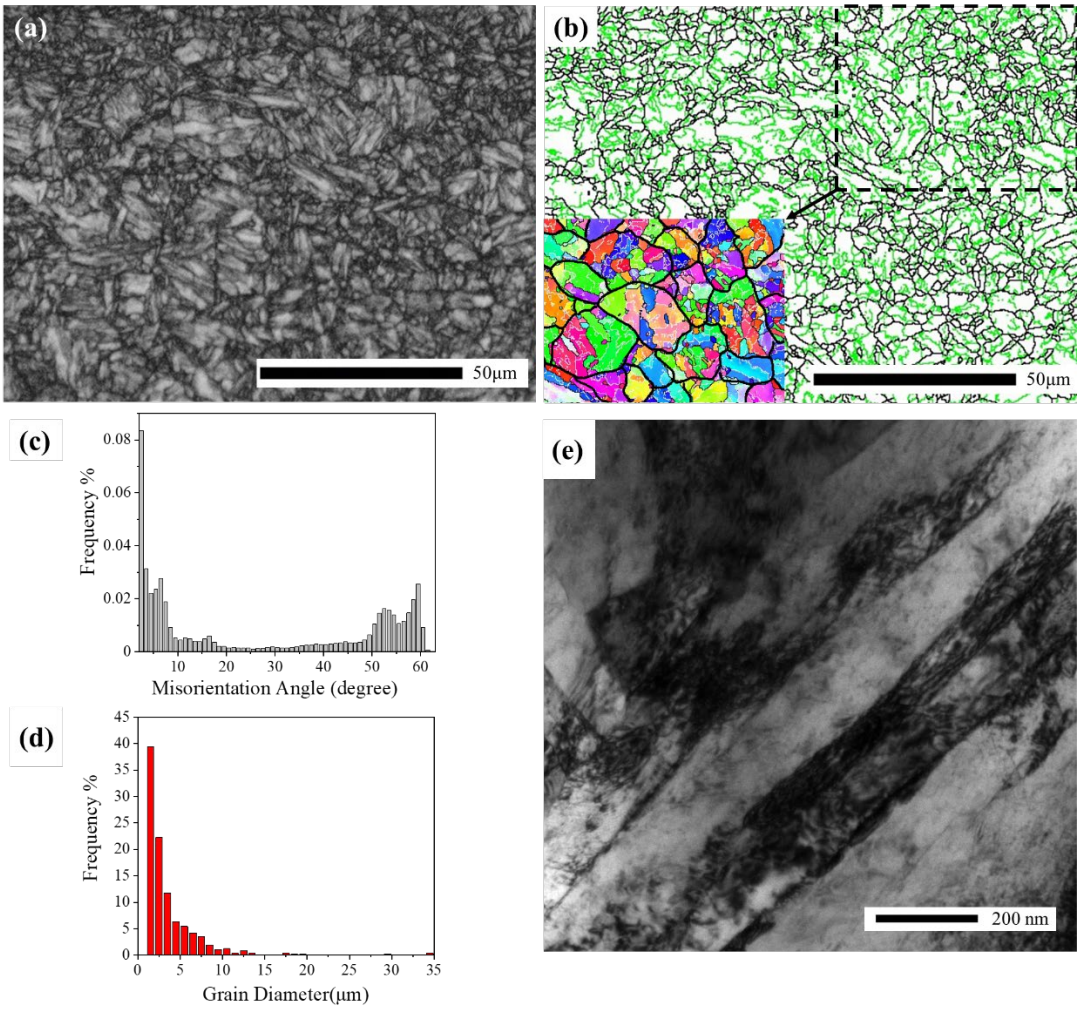

Fig. 5. EBSD and TEM images of AG525 steel. (a) band contrast map, (b) misorientation map of grain boundaries, (c) misorientation angle distribution, (d) grain size distribution, (e) TEM micrograph of the fine structure.

To verify the dislocation density of AG525, the kernel average misorientation (KAM) map and local misorientation angle distribution of AG525 is shown in Fig. 6. The average misorientation angle in the KAM map is ~1.02°. In general, most residual dislocation can be considered as geometrically necessary dislocations to accommodate local strain [33]. As a result, the residual dislocation density, ρ_{GND}, which is directly related to the local misorientation, Θ, can be estimated by the following approach [34, 35]:

$$\rho_{GND} = \frac{2\Theta}{ub} \quad (3)$$

where u = 300 nm is the unit length of a circuit around a specific point of interest (which is equal to the scanning step length), b = 0.25 nm is the magnitude of Burgers vector for iron, and Θ = 1.02° is evaluated from the local misorientation profile in the KAM map. The calculated density of residual dislocations in the steel is 4.75× 10^{14} m^{-2}, which is consistent with the dislocation densities calculated by XRD.

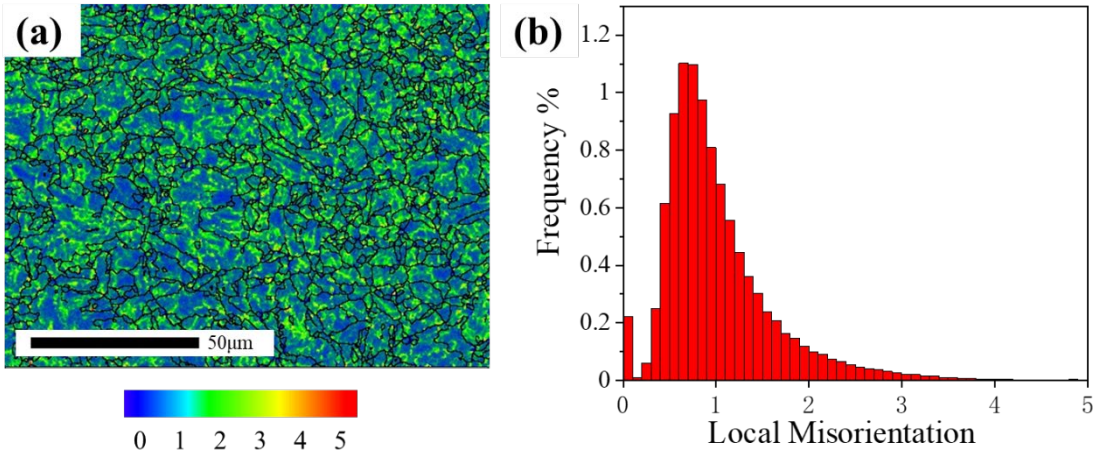

Fig. 6. Kernel average misorientation map.

3.4 Nanoscale precipitates

In order to examine the nanoscale precipitates of SS and AG525 steel, APT studies were carried out. The APT 3D reconstructions of the SS (Fig.7a) show a homogenous distribution of all atoms in the APT tip, revealing neither the existence of Cu nor carbide precipitates. The APT 3D reconstructions of AG525 are presented in Fig. 7b. The Cu-rich precipitates in AG525 have a rod-like structure with a cross-sectional radius of ~3.2 nm and a length of ~20 nm. The length directions of all rod-shaped

precipitation are the same. The number density of Cu-rich precipitates is approximately $5.3\times10^{22}/m^3$, corresponding to a volume fraction of 1.56%. The proximity histograms depicting the composition of the Cu-rich precipitates are plotted in Fig. 7(c). The Cu-rich precipitates are enriched with a high level of Cu about 50 at.% at the center. A diffuse segregation of Ni (3-5 at.%) and Mn (1-3 at.%) can be determined at the interface between the Cu-rich precipitates and the matrix.

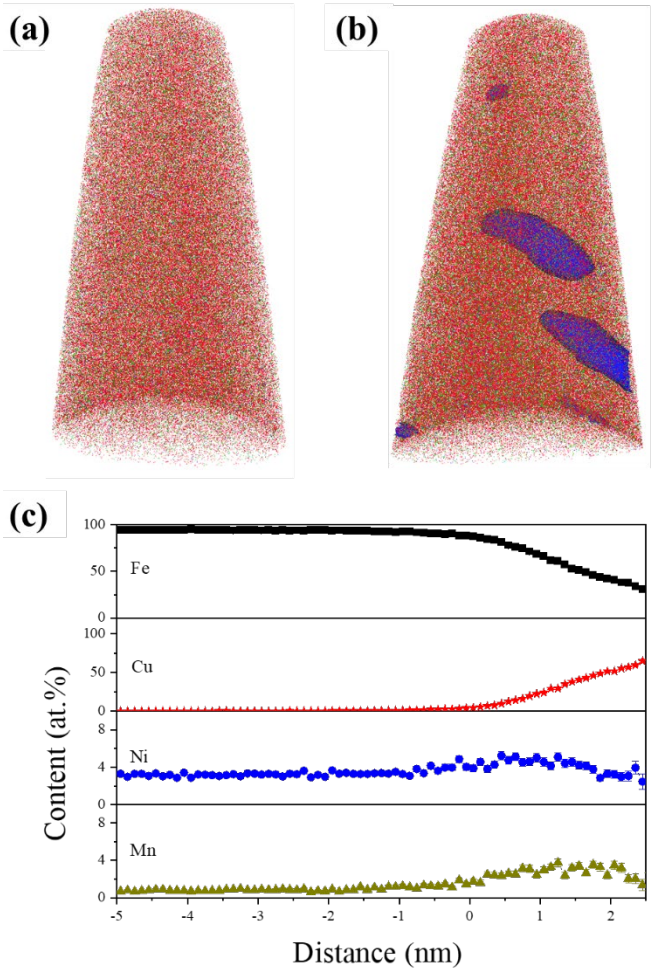

Fig. 7. APT 3D reconstructions of SS (a) and AG525 (b) at 10 at.% Cu iso-concentration surfaces; (c) proximity histograms of Cu-rich precipitates in AG525 steel.

4. Discussion

4.1 Strengthening mechanisms

To understand the strengthening mechanisms of the steels with and without Cu-rich nanoprecipitates, all strengthening components contributing to yield strength are carefully examined, including the solid-solution strengthening (σ_{ss}), grain boundary strengthening (σ_{GB}), dislocation strengthening (σ_{dislo}), and precipitation strengthening (σ_{ppt}). The yield strength can be evaluated by cumulating the strength for various individual strengthening methods [13, 36]:

$$\sigma = \sigma_{GB} + \sigma_{ss} + \sigma_{dislo} + \sigma_{ppt} \quad (4)$$

The grain boundary strengthening can be described by Hall-Petch equation:

$$\sigma_{GB} = \sigma_0 + k_y d^{-\frac{1}{2}} \quad (5)$$

where σ_0 is the friction stress with the value of 50 MPa [13, 37], and k_y = 600 MPa μm$^{1/2}$ is the Hall-Petch coefficient of HSLA steels [38]. Since it is hard for the LAGBs to migrate at low aging temperature, we suppose that the EGS of SS and AG525 does not change. With the effective grain size, d = 3.57 μm in SS and AG525 steels, the strength contributed by grain boundary strengthening can be estimated as 367 MPa for both SS and AG525 steels.

Solid solution strengthening can be expressed as follows [39]:

$$\sigma_{ss} = 4570[C] + 37[Mn] + 83[Si] + 38[Cu] + 11[Mo] + 0[Ni] - 30[Cr] \quad (6)$$

where $[Xi]$ is the content of element X_i dissolved in the steel, in wt.%. Based on the concentration of the matrix determined by APT, the contribution by solid solution is estimated as 139 MPa for AG525 steel and 178 MPa for SS steel. The low value for AG525 steel can be attributed to the low Cu concentration in the matrix in AG525 steel after aging.

The dislocation strengthening can be evaluated as follows [33, 40]:

$$\sigma_{dislo} = M\alpha Gb\sqrt{\rho} \quad (7)$$

where α = 0.2 is a constant, M = 3.0 is the Taylor factor, G = 80 GPa is the shear modulus of α-Fe matrix and b = 0.25 nm is the Burgers vector of dislocations in the α-Fe matrix. The strength contributed by dislocation strengthening is estimated as 361 and 264 MPa for SS and AG525, respectively.

Cu-rich precipitates tend to form the elongated rod-like morphologies to reduce the interfacial energy. This is consistent to some previous observations [19, 41-43]. Therefore, The effective ellipsoid radius based on a sphere of the same total volume as the ellipsoid can be calculated from [44]:

$$r_{ellipsoid} = \sqrt[3]{(r_{major})(r_{minor1})(r_{minor2})} \quad (8)$$

The effective ellipsoid radius of these Cu precipitates in AG525 is calculated to be ~4.7 nm. Due to the large size of Cu-rich precipitates in

AG525 sample, it is believed that Orowan strengthening plays the most important role through Orowan looping mechanism [45]:

$$\Delta\sigma_{Orowan} = 0.1Gb\frac{f^{1/2}}{R}\ln\frac{R}{b} \quad (9)$$

where f is the volume fraction of the nanoscale precipitates (f = 0.03) and R is the mean precipitate radius ($r_{ellipsoid}$ = 4.7 nm). The contribution from Orowan strengthening is calculated to be 156 MPa.

The contribution from each strengthening mechanism, derived from above equations, are summarized in Table 3 and plotted in Fig. 8. It can be seen that the estimated strength for both SS and AG525 steel are in good agreement with the tested values, confirming the validity of the estimation. It is evident that after aging, precipitation strengthening from Cu-precipitates contributes an extra strength of ~156 MPa, as compared to the SS steel. However, the contributions from both the solid-solution strengthening and dislocation strengthening are reduced. Thus, the total increment in yield strength is around ~20 MPa after aging.

Table 3. Contributions of the various strengthening mechanisms to the yield strength of the SS and AG525 steel

	Tested value (MPa)	Calculated value (MPa)	σ_{GB} (MPa)	σ_{ss} (MPa)	σ_{dislo} (MPa)	σ_{ppt} (MPa)
SS	905	906	367	178	361	-
AG525	927	924	367	139	262	156

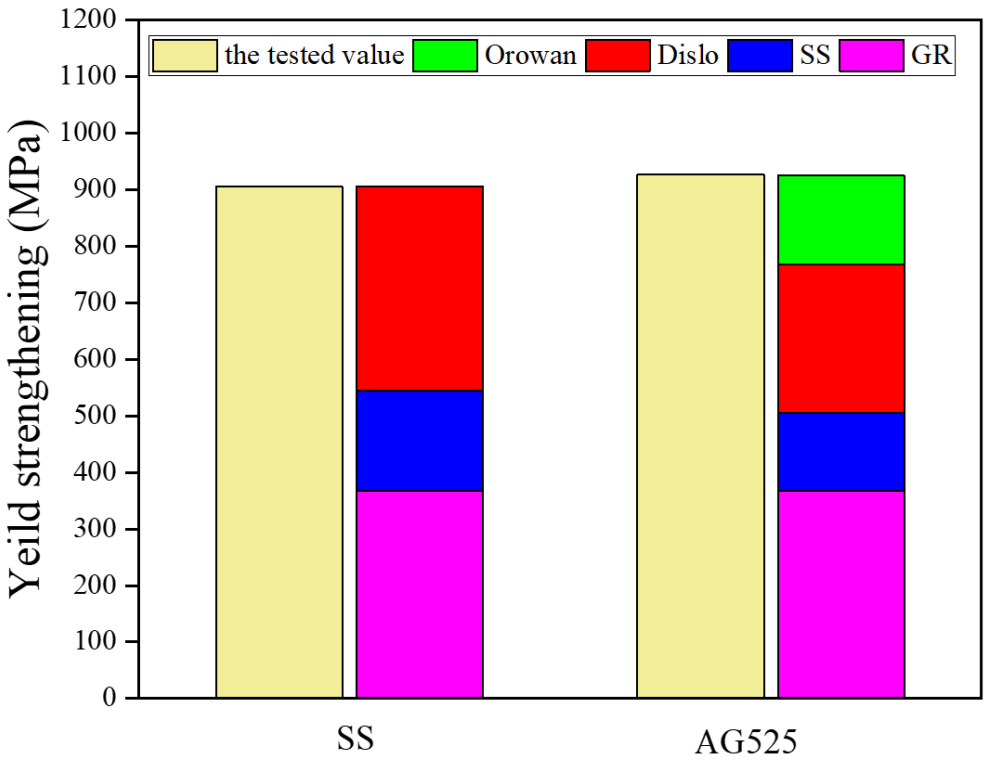

Fig. 8. Contributions of the various strengthening mechanisms to the yield strength of the SS and AG525 steel.

4.2 Toughening mechanisms

Impact toughness is an important design criterion for many engineering applications. Temper embrittlement is one of the major causes for reduced impact toughness in ferritic and martensitic steels due to the segregation of impurities along the prior austenite grain boundaries [8, 14, 15]. These impurities weaken the grain boundaries and cause intergranular fracture, which can significantly reduce the impact toughness [46]. However, only ductile fracture and transgranular cleavage fracture occurred in AG525 at various temperatures. It shows that there is no temper-embrittlement in AG525 steel. This is mainly due to the uniform distribution of the Cu precipitates in steel. The other reason is that there are

no brittle phases or impurities at the grain boundaries.

As the impact temperature decreases, the steel gradually transforms from ductile to brittle fracture. However, the crack initiation energy does not change significantly (Tab. 2). For both SS and AG525 samples, with the decrease in temperature, the crack unstable propagation stage begins to appear in the process of crack propagation, and the crack stable propagation stage gradually decreases, indicating that the crack propagation is the main factor affecting DBTT. The microstructure of the lath martensite has significant effects on the propagation of cleavage crack due to its hierarchical structure [30, 47]. The structure of the fine lath martensite can increase crack resistance at the preliminary stage of crack propagation and delay the rapid unstable crack propagation. When cracks intersect block/packet boundaries of martensite, the cracks can be blunted due to the misorientations of cleavage planes at the block boundaries [48]. Fig. 9 is the schematic diagram showing such a multi-level structure of martensite. Lath martensite consists of hierarchically arranged substructures within a prior-austenite grain (PAG), namely the packets and blocks of laths. A block contains laths with the same orientation, while a packet is a group of blocks with the same habit plane. The lath boundaries are LAGBs while the packet and block boundaries are HAGBs. These are the main reasons for the low DBTT of SS. The excellent low temperature toughness of SS and AG525 is mainly due to the hierarchical structure of

lath martensite.

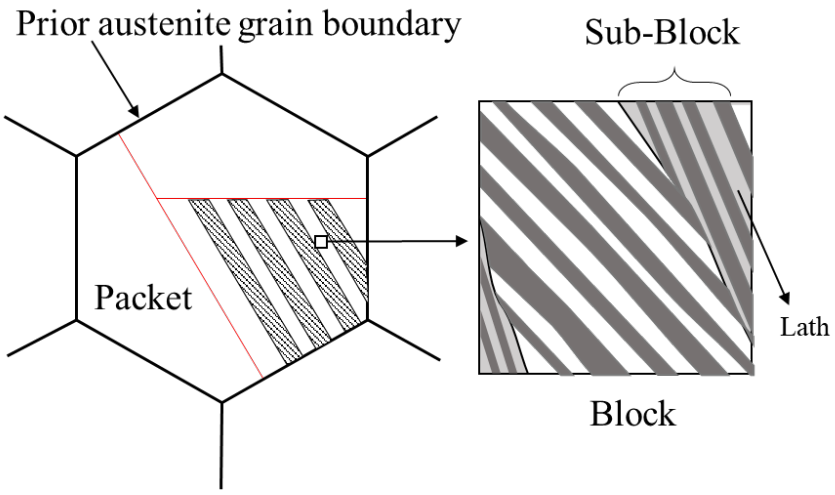

Fig. 9 The illustration of multi-level microstructures for lath martensite

It is generally believed that the lath martensite is polygonized after tempering, and the lath structure is destroyed [8]. In this study, we found that AG525 still retains the lath martensitic structure after aging at 525 °C. EBSD and SEM results clearly reveal the typical hierarchical structure of lath martensite in AG525, as shown in Fig. (5). This is because the addition of Mo, Cr, Ti, and Nb significantly improves the tempering resistance of steel and reduces the speed of recovery [49].

Compared with AG525, the SS has a higher upper shelf energy and a lower DBTT. The higher upper shelf energy is due to the higher dislocation density of SS. Higher dislocation density leads to higher work hardening, which leads to higher peak loads and higher crack initiation work as shown in Table 2.

The basic parameter to control the crack fracture mode is the stress intensity, K, which characterizes the degree of the stress concentration

around a loaded crack [50, 51]. If the stress intensity at the crack-tip K_{tip} exceeds the critical value required for fracture (the Griffith value for a mode I crack, K_{IC}), the material will fracture in a brittle manner [52]. A model for crack tip plasticity was proposed by Hartmaier [53, 54] and Roberts [55, 56], as shown in Fig.10. Their models make use of a global, externally applied load, K_{app}, and a local, effective stress intensity, K_{eff}, at the crack tip. If the effective stress intensity ($K_{eff} = K_{app} - K_{dis}$) reaches the critical stress intensity, then fracture will occur ($K_{eff} = K_{IC}$). If K_{eff} never reaches K_{IC} for any applied load, then the material shows ductile behavior [51]. The nucleation of dislocations takes place in the vicinity of the crack tip where dislocations are emitted from dipole sources. Image forces make them glide to the crack tip free surface where they are annihilated and thus cause crack tip blunting. Dislocations that glide away from the crack tip are so called shielding dislocations [57]. If sufficient dislocation activity occurs, the high level of K_{dis} can keep K_{tip} below the value required for fracture, so that condition is never satisfied and the material is then ductile. The DBTT in bcc metals is determined by the differences of the mobile dislocation density in front of the crack tip.

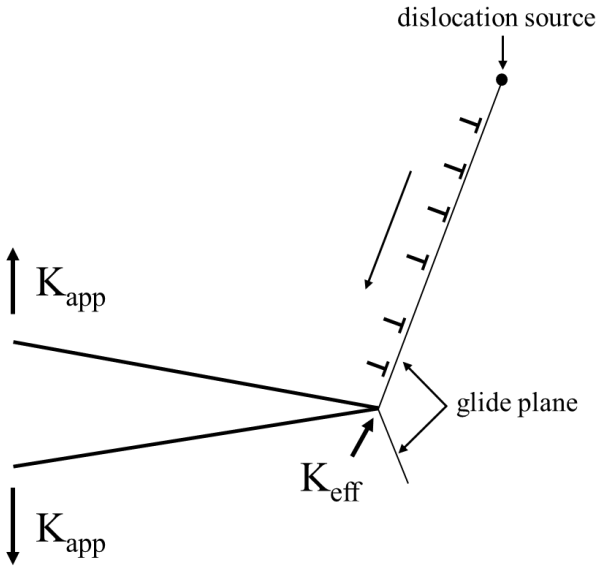

Fig. 10 A model for crack tip plasticity [53]

Ashby and Embury proposed that k_{eff} decreases with the increase in dislocation density [58]. The dislocation density in SS sample is higher than that in AG525. Thus, AG525 sample has a higher k_{eff}, which is more prone to occur crack unstable propagation, leading to a higher DBTT.

5. Summary

Based on the systematic studies on the tensile properties, microstructure, strengthening mechanisms and the DBTT of the newly developed steel, the following conclusions can be drawn:

(1) A high strength steel with a combination of 167 J/cm^2 V-notch impact toughness at −80 °C, a 927MPa yield strength and a 21% total elongation were obtained. The DBTT is −91 °C and the upper shelf energy is 216 J.

(2) The microstructure of the SS sample is lath martensite with a high

dislocation density. After aging, the dislocation density decreases and large amounts of Cu-rich precipitates emerge, while the lath martensite structure and EGS of steel remains unchanged.

(3) In SS steel, the strengthening mechanism includes solid-solution strengthening (178 MPa), dislocation strengthening (361 MPa) and grain boundary strengthening (367 MPa). After aging, precipitation strengthening from Cu-precipitates contributes an extra strengthening of ~156 MPa, and both of the solid-solution strengthening and dislocation strengthening are reduced. The total increment in yield strength is around ~20 MPa after aging.

(4) Crack propagation is the main factor affecting DBTT, and fine lath martensite can increase crack resistance at the preliminary stage of crack propagation and delay the rapid unstable crack propagation. Higher dislocation density leads a higher crack initiate energy and a lower k_{eff}, which is less prone to occur crack unstable propagation, leading to a lower DBTT.

Acknowledgments

The present work was supported by the National Key Research and Development Project (2018YFE0115800), the Fundamental Research Funds for the Central Universities (3072020CFT1005), Heilongjiang Touyan Innovation Team Program, Innovation Center of Nuclear Materials for National Defense Industry (HCL-08). Atom probe tomography research was conducted with the assistance of Dr. J. H. Luan and Dr. Z. B. Jiao at the Inter-University 3D Atom Probe Tomography Unit of City University of Hong Kong supported by the NSFC grant 51801169, CityU grant 9360161 and CRF grant C1027-14E.

References

[1] A. Wilson, E. Hamburg, D. Colvin, S. Thompson, G. Krauss, Properties and microstructures of copper precipitation aged plate steels, Microalloyed HSLA steels (1988) 259-275.

[2] E.J. Czyryca, R.E. Link, R.J. Wong, D.A. Aylor, T.W. Montem, J.P. Gudas, Development and certification of HSLA-100 steel for naval ship construction, Naval engineers journal 102(3) (1990) 63-82.

[3] B. Graville, Welding of HSLA (Microalloyed) Structural Steels, ASM, Metals Park, OH 85 (1978).

[4] S.W. Thompson, Interrelationships between yield strength, low-temperature impact toughness, and microstructure in low-carbon, copper-precipitation-strengthened, high-strength low-alloy plate steels, Materials Science and Engineering: A 711 (2018) 424-433.

[5] D.C. Saha, E. Biro, A.P. Gerlich, Y. Zhou, Martensite tempering kinetics: Effects of dislocation density and heating rates, Materials Characterization 168 (2020) 110564.

[6] L.Y. Wang, Y.X. Wu, W.W. Sun, Y. Bréchet, L. Brassart, A. Arlazarov, C.R. Hutchinson, Strain hardening behaviour of as-quenched and tempered martensite, Acta Materialia 199 (2020) 613-632.

[7] S.-W. Young, M. Sato, K. Yamamitsu, Y. Shimada, Y. Zhang, G. Miyamoto, T. Furuhara, Effect of Alloying Elements on the High-Temperature Tempering of Fe-0.3N Martensite, Acta Materialia 206 (2021) 116612.

[8] Krauss, G.J.S.R. International, Tempering of Lath Martensite in Low and Medium Carbon Steels: Assessment and Challenges, (2017) 1700038.

[9] S. Jiang, H. Wang, Y. Wu, X. Liu, H. Chen, M. Yao, B. Gault, D. Ponge, D. Raabe, A. Hirata, M. Chen, Y. Wang, Z. Lu, Ultrastrong steel via minimal lattice misfit and high-density nanoprecipitation, Nature 544(7651) (2017) 460-464.

[10] Z. Jiao, J. Luan, Z. Zhang, M.K. Miller, W. Ma, C. Liu, Synergistic effects of Cu and Ni on nanoscale precipitation and mechanical properties of high-strength steels, Acta materialia 61(16) (2013) 5996-6005.

[11] S. Xu, Y. Zhao, D. Chen, L. Sun, L. Chen, X. Tong, C. Liu, Z. Zhang, Nanoscale precipitation and its influence on strengthening

mechanisms in an ultra-high strength low-carbon steel, International Journal of Plasticity 113 (2019) 99-110.

[12] S.S. Xu, Y. Zhao, X. Tong, H. Guo, L. Chen, L.W. Sun, M. Peng, M.J. Chen, D. Chen, Y. Cui, G.A. Sun, S.M. Peng, Z.W. Zhang, Independence of work hardening and precipitation strengthening in a nanocluster strengthened steel, Journal of Alloys and Compounds 712 (2017) 573-578.

[13] T. Liu, Z. Cao, H. Wang, G. Wu, J. Jin, W. Cao, A new 2.4 GPa extra-high strength steel with good ductility and high toughness designed by synergistic strengthening of nano-particles and high-density dislocations, Scripta Materialia 178 (2020) 285-289.

[14] H.J. Kong, C.T. Liu, A review on nano-scale precipitation in steels, Technologies 6(1) (2018) 36.

[15] S.K. Dhua, A. Ray, D.S. Sarma, Effect of tempering temperatures on the mechanical properties and microstructures of HSLA-100 type copper-bearing steels, Materials Science and Engineering: A 318(1) (2001) 197-210.

[16] J.B. Rellick, C.J. McMahon, Intergranular embrittlement of iron-carbon alloys by impurities, Metallurgical Transactions 5(11) (1974) 2439-2450.

[17] M. Kuzmina, D. Ponge, D. Raabe, Grain boundary segregation engineering and austenite reversion turn embrittlement into toughness:

Example of a 9wt.% medium Mn steel, Acta Materialia 86 (2015) 182-192.

[18] D. Jain, D. Isheim, A.H. Hunter, D.N. Seidman, Multicomponent High-Strength Low-Alloy Steel Precipitation-Strengthened by Sub-nanometric Cu Precipitates and M2C Carbides, Metallurgical and Materials Transactions A 47(8) (2016) 3860-3872.

[19] D. Jain, D. Isheim, D.N. Seidman, Carbon redistribution and carbide precipitation in a high-strength low-carbon HSLA-115 steel studied on a nanoscale by atom probe tomography, Metallurgical and Materials Transactions A 48(7) (2017) 3205-3219.

[20] M. Kapoor, D. Isheim, S. Vaynman, M.E. Fine, Y.W. Chung, Effects of increased alloying element content on NiAl-type precipitate formation, loading rate sensitivity, and ductility of Cu- and NiAl-precipitation-strengthened ferritic steels, Acta Materialia 104 (2016) 166-171.

[21] W. Hou, Q. Liu, J. Gu, Improved impact toughness by multi-step heat treatment in a 1400 MPa low carbon precipitation-strengthened steel, Materials Science and Engineering: A 797 (2020) 140077.

[22] H.J. Kong, C. Xu, C.C. Bu, C. Da, J.H. Luan, Z.B. Jiao, G. Chen, C.T. Liu, Hardening mechanisms and impact toughening of a high-strength steel containing low Ni and Cu additions, Acta Materialia 172 (2019) 150-160.

[23] Z.J. Xie, S.F. Yuan, W.H. Zhou, J.R. Yang, H. Guo, C.J. Shang,

Stabilization of retained austenite by the two-step intercritical heat treatment and its effect on the toughness of a low alloyed steel, Materials & Design 59 (2014) 193-198.

[24] L.Y. Kan, Q.B. Ye, Q.H. Wang, Y. Tian, Z.D. Wang, Y.M. Wang, J. Hu, Refinement of Cu-M2C precipitates and improvement of strength and toughness by Ti microalloying in a Cu-bearing steel, Materials Science and Engineering: A 802 (2021) 140678.

[25] G.K. Williamson, W.H. Hall, X-ray line broadening from filed aluminium and wolfram, Acta Metallurgica 1(1) (1953) 22-31.

[26] G.K. Williamson, R.E.J.P.M. Smallman, III. Dislocation densities in some annealed and cold-worked metals from measurements on the X-ray debye-scherrer spectrum, 1(1) (1956) 34-46.

[27] Y. Sakai, K. Tamanoi, N. Ogura, Application of tanh curve fit analysis to fracture toughness data of Japanese RPVS, Nuclear Engineering and Design 115(1) (1989) 31-39.

[28] H. Ma, L. Zhu, Z. Wang, UNIFIED CORRELATIONS IN TRANSITION TEMPERATURES OF LOW ALLOY STEELS AND WELD METALS OF VARIOUS TOUGHNESSES, Fatigue & Fracture of Engineering Materials & Structures 19(12) (1996) 1459-1470.

[29] B., Tanguy, and, J., Besson, and, R., Piques, and, A.J.E.F. Mechanics, Ductile to brittle transition of an A508 steel characterized by Charpy impact test: Part II: modeling of the Charpy transition curve, 72(3)

(2005) 413-434.

[30] H. Luo, X. Wang, Z. Liu, Z. Yang, Influence of refined hierarchical martensitic microstructures on yield strength and impact toughness of ultra-high strength stainless steel, Journal of Materials Science & Technology 51 (2020) 130-136.

[31] B. Hutchinson, J. Hagström, O. Karlsson, D. Lindell, M. Tornberg, F. Lindberg, M. Thuvander, Microstructures and hardness of as-quenched martensites (0.1–0.5% C), Acta Materialia 59(14) (2011) 5845-5858.

[32] H.T. Wang, Y. Tian, Q.B. Ye, R.D.K. Misra, Z.D. Wang, G.D. Wang, Determining role of microstructure on crack arrest and propagation phenomenon in low-carbon microalloyed steel, Materials Science and Engineering: A 761 (2019) 138009.

[33] H. Pan, R. Kang, J. Li, H. Xie, Z. Zeng, Q. Huang, C. Yang, Y. Ren, G. Qin, Mechanistic investigation of a low-alloy Mg–Ca-based extrusion alloy with high strength–ductility synergy, Acta Materialia 186 (2020) 278-290.

[34] H. Gao, Y. Huang, W.D. Nix, J.W. Hutchinson, Mechanism-based strain gradient plasticity— I. Theory, Journal of the Mechanics and Physics of Solids 47(6) (1999) 1239-1263.

[35] L.P. Kubin, A. Mortensen, Geometrically necessary dislocations and strain-gradient plasticity: a few critical issues, Scripta Materialia 48(2)

(2003) 119-125.

[36] J.S. Wang, M.D. Mulholland, G.B. Olson, D.N. Seidman, Prediction of the yield strength of a secondary-hardening steel, Acta Materialia 61(13) (2013) 4939-4952.

[37] X. Zhang, A. Godfrey, X. Huang, N. Hansen, Q. Liu, Microstructure and strengthening mechanisms in cold-drawn pearlitic steel wire, Acta Materialia 59(9) (2011) 3422-3430.

[38] S. Takaki, K. Kawasaki, Y. Kimura, Mechanical properties of ultra fine grained steels, Journal of Materials Processing Technology 117(3) (2001) 359-363.

[39] F.B. Pickering, Physical Metallurgy and the Design of Steels, Applied Science Publishers1978.

[40] X. Zhang, N. Hansen, Y. Gao, X. Huang, Hall–Petch and dislocation strengthening in graded nanostructured steel, Acta Materialia 60(16) (2012) 5933-5943.

[41] Z. Zhang, C.T. Liu, M.K. Miller, X.-L. Wang, Y. Wen, T. Fujita, A. Hirata, M. Chen, G. Chen, B.A. Chin, A nanoscale co-precipitation approach for property enhancement of Fe-base alloys, Scientific reports 3 (2013) 1327.

[42] P. Othen, M. Jenkins, G. Smith, High-resolution electron microscopy studies of the structure of Cu precipitates in α-Fe, Philosophical magazine A 70(1) (1994) 1-24.

[43] R. Prakash Kolli, D.N. Seidman, The temporal evolution of the decomposition of a concentrated multicomponent Fe–Cu-based steel, Acta Materialia 56(9) (2008) 2073-2088.

[44] R.A. Karnesky, C.K. Sudbrack, D.N. Seidman, Best-fit ellipsoids of atom-probe tomographic data to study coalescence of γ′ (L12) precipitates in Ni–Al–Cr, Scripta Materialia 57(4) (2007) 353-356.

[45] E.I. Galindo-Nava, W.M. Rainforth, P.E.J. Rivera-Díaz-del-Castillo, Predicting microstructure and strength of maraging steels: Elemental optimisation, Acta Materialia 117 (2016) 270-285.

[46] K. Godbole, C.R. Das, S.K. Albert, B.B. Panigrahi, Grain boundary engineering to overcome temper embrittlement in martensitic steel, Materials Letters 264 (2020) 127321.

[47] Y. Zhao, X. Tong, X.H. Wei, S.S. Xu, S. Lan, X.L. Wang, Z.W.J.I.J.o.P. Zhang, Effects of microstructure on crack resistance and low-temperature toughness of ultra-low carbon high strength steel, (2019).

[48] Q., Zikry, A.J.E.F.M. M., Dynamic fracture predictions of microstructural mechanisms and characteristics in martensitic steels, (2015).

[49] K. Maruyama, K. Sawada, J.I.J.I.I. Koike, Strengthening Mechanisms of Creep Resistant Tempered Martensitic Steel, 41(6)(6) (2001) 641--653.

[50] Z. Mengqi, Y. Shanwu, W.J.M.o.m. Farong, Competition

mechanism of brittle-ductile transition of metals under tensile condition, 137(Oct.) (2019) 103138.1-103138.6.

[51] E. Tarleton, S.G.J.P.M. Roberts, Dislocation dynamic modelling of the brittle-ductile transition in tungsten, 89(31) (2009) 2759-2769.

[52] B. Gurrutxaga-Lerma, D.S. Balint, D. Dini, A.P.J.J.o.t.M. Sutton, P.o. Solids, A Dynamic Discrete Dislocation Plasticity study of elastodynamic shielding of stationary cracks, 98 (2017) 1-11.

[53] A. Hartmaier, P.J.P.R.B. Gumbsch, Thermal activation of crack-tip plasticity: The brittle or ductile response of a stationary crack loaded to failure, 71(2) (2005) 308–312.

[54] A. Hartmaier, P.J.P.M.A. Gumbsch, Scaling relations for crack-tip plasticity, 82(17) (2002) 3187-3200.

[55] S.G. Roberts, Modelling the Brittle to Ductile Transition in Single Crystals, 1996.

[56] S.G. Roberts, P.B. Hirsch, A.S. Booth, M. Ellis, F.C.J.P.S. Serbena, Dislocations, cracks and brittleness in single crystals, 1993 (1993) 420.

[57] C. Bonnekoh, U. Jäntsch, J. Hoffmann, H. Leiste, A. Hartmaier, D. Weygand, A. Hoffmann, J. Reiser, The brittle-to-ductile transition in cold rolled tungsten plates: Impact of crystallographic texture, grain size and dislocation density on the transition temperature, International Journal of Refractory Metals and Hard Materials 78 (2019) 146-163.

[58] M.F. Ashby, J.D.J.S.M. Embury, The influence of dislocation density on the ductile-brittle transition in BCC metals, 19(4) (1985) 557-562.